applied sciences

MDPI

Article

A Group Theoretic Analysis of Mutual Interactions of Heat and Mass Transfer in a Thermally Slip Semi-Infinite Domain

Khalil Ur Rehman [1,2,*], Wasfi Shatanawi [1,3,*], Kamaleldin Abodayeh [1] and Taqi A. M. Shatnawi [4]

[1] Department of Mathematics and Sciences, College of Humanities and Sciences, Prince Sultan University, Riyadh 11586, Saudi Arabia; kamal@psuu.edu.sa
[2] Department of Mathematics, Air University, PAF Complex E-9, Islamabad 44000, Pakistan
[3] Department of Medical Research, China Medical University Hospital, China Medical University, Taichung 40402, Taiwan
[4] Department of Mathematics, Faculty of Science, The Hashemite University, Zarqa 13133, Jordan; taqi_shatnawi@huu.edu.jo
* Correspondence: kurrehman@psu.edu.sa (K.U.R.); wshatanawi@psu.edu.sa (W.S.)

Abstract: Group theoretic analysis is performed to get a new Lie group of transformations for non-linear differential systems constructed against mass and heat transfer in the thermally magnetized non-Newtonian fluid flow towards a heated stretched porous surface. The energy equation is used with additional effects, namely heat sink and heat source. The chemical reaction is also considered by the use of the concentration equation. The symmetry analysis helps us in numerical computations of surface quantities for (i) permeable and non-permeable surfaces, (ii) thermal slip and non-thermal slip flows, (iii) magnetized and non-magnetized flows, (iv) chemically reactive and non-reactive flows. For all these cases, the concerned emerging partial differential system is transformed into a reduced ordinary differential system and later solved numerically by using the shooting method along with the Runge-Kutta scheme. The observations are debated graphically, and numerical values are reported in tabular forms. It is noticed that the heat transfer rate increases for both the thermal slip and non-slip cases. The skin friction coefficient declines towards the Weissenberg number in the magnetized field.

Keywords: heat transfer; mass transfer; Lie symmetry; thermal slip; heat source/sink; magnetized flow

Citation: Rehman, K.U.; Shatanawi, W.; Abodayeh, K.; Shatnawi, T.A.M. A Group Theoretic Analysis of Mutual Interactions of Heat and Mass Transfer in a Thermally Slip Semi-Infinite Domain. *Appl. Sci.* **2022**, *12*, 2000. https://doi.org/10.3390/app12042000

Academic Editor: Jeong Ik Lee

Received: 29 December 2021
Accepted: 8 February 2022
Published: 14 February 2022

1. Introduction

Materials processing, power generation, transportation, civil infrastructure, food production, automobiles, and hydroelectric power plants, to mention just a few, are the dominant parts of fluid mechanics applications. Owning such a vital role in fluid science, mathematicians, oceanographers, geologists, biologists, atmospheric scientists, physicists, and engineers pay attention to fluid flow fields. For example, the heat transmission characteristics of a visco-elastic fluid flow by way of a stretched surface carrying a heat sink and heat source were examined using mathematical analysis by Vajravelu and Rollins [1]. In terms of Kummer's and parabolic cylinder functions, solutions for heat transfer rate and temperature towards the Prandtl number were obtained. For small Prandtl numbers, it was demonstrated that there was no boundary layer in the solution. A mathematical analysis of heat and momentum for flow towards a stretched surface was performed by Andersson et al. [2]. Accurate similarity transformations were carried out to diminish the flow of time-dependent equations to ordinary differential equations. For certain iterations of an unsteadiness parameter and Prandtl number, the resulting problem was numerically solved. The temperature grew monotonically towards the ambient field. The visco-elastic heat and flow properties subject to the porous stretched medium were considered by Abel et al. [3]. Temperature-dependent viscosity was considered. Such assumption results

in non-linear equations. Such involved equations were solved numerically. The impact of visco-elastic permeability parameters and fluid viscosity towards numerous conditions were investigated for two separate scenarios, namely heat flux (PHF) and prescribed surface temperature (PST). In this examination, the most noteworthy discovery was that the skin friction admits an inverse relation towards the permeability parameter. The magnetized heat transmission over a stretched sheet in the visco-elastic fluid was investigated by Zakaria [4]. The successive approximation approach was used to get the solution of flow equations. On the temperature and velocity, the impacts of relaxation time parameter, Prandtl number, Alfven velocity, surface mass transfer, and elastic velocity coefficients were debated graphically. The heat and flow aspects of a second-grade liquid towards a stretched surface were investigated by Cortell [5]. The order reduction of the involved flow equations was conducted via similarity transformations. The energy equation with viscous dissipation was considered, and the variation in both temperature gradient and temperature was investigated. Abel and Mahesha [6] investigated magnetized a visco-elastic liquid towards a sheet with the assumptions of a heat source that is non-uniform with thermal radiation. The thermal conductivity was believed to change with temperature in a linear fashion. The primary flow equations were partial differential equations (PDEs), which were later reduced as ordinary differential equations (ODEs) by using the appropriate transformations. The regular perturbation scheme was used to solve the altered equations. The efficient shooting method also yielded a numerical solution, which agrees well with the analytical answer. In several plots, the various flow variables that determine temperature profiles, such as heat sink/source, thermal radiation, and visco-elastic parameters, Eckert, Prandtl, and Chandrasekhar numbers, were shown, and the rate of heat transfer coefficients was also measured against these parameters. By considering heat sink/source, viscous dissipation, and magnetic field, an analysis was performed to examine the convective flow having an exponentially stretched plate and temperature regime. The extremely non-linear momentum and energy equations have approximate analytical similarity solutions. The current findings admitted great accord with the existing work on a variety of special instances. For various values of the governing parameters, heat transfer rate and temperature regimes were examined. On the directional flow coordinate, numerical solutions were derived towards exponentially stretched velocity. The implications of numerous physical parameters on dimensionless heat transfer characteristics, such as Prandtl number, Hartman number, and Grashof number, were thoroughly examined. It was discovered that increasing the Prandtl number lowers the drag faced by fluid while increasing the magnetic field strength raises the local Nusselt number. By considering heat transfer, volumetric heating, magnetic field, and a variety of other factors, the flow of a visco-elastic fluid over a porous stretched surface was considered by Pal [7]. It was demonstrated that their solutions do not appear to have emerged earlier and can be developed by making careful picks of the involved functions. On a stretching sheet, the pseudoplastic flow field was investigated by Ashrafi and Meysam [8]. The flow equations were converted into lower-order equations via transformations. After that, the system was numerically integrated with the RK scheme. The impact of various flow variables, such as heat transfer coefficient, apparent viscosity, temperature, velocity, towards Prandtl number, pseudo-plasticity index, and unsteadiness parameter, were studied in depth. The stretched surface was used by Zhang et al. [9] to explore heat transfer aspects of Oldroyd-B fluid with suspended nanoparticles. Here, with Ag and Cu, the polyvinyl alcohol is treated as a base fluid. The stretched sheet velocity and temperature were supposed to vary. The flow equations were first constructed, and the similarity transformation was used to convert them to ODEs. The homotopy analysis method (HAM) was used to derive the analytical answers, which exhibit good agreement with earlier results. For analyzing the heat transmission of fractional visco-elastic magneto-hydrodynamics (MHD) fluid flow field, the Lie group was introduced by Chen et al. [10]. The Grünwald scheme approximation was used to minimize and solve fractional equations conjectured with Riemann–Liouville operators numerically. The results reveal that the wall stretching exponent, fractional derivative, and magnetic field all have a significant impact

on skin friction and heat conductivity. For high fractional-order derivatives, visco-elastic fluids move faster and do not stick near the outer flow. As the magnetic field parameter is increased, skin friction increases, while heat transmission decreases. Refs. [11–30] can be used to examine past and recent trends. Besides this, heat transmission and transport phenomena in porous media are significant processes in many technical applications, including heat pipe technology, chemical catalytic reactors, electronic cooling, pack-sphere bed, and heat exchangers, to name a few. Heat transport in the porous fibrous medium is a well-known and complicated subject that has received a lot of attention. Many drying and heating uses of such materials require a detailed grasp of this challenge. Similarly, several textile materials and, more recently, ovens that are utilized as heat barrier materials are being investigated. As a result, due to its ever-increasing applications in industries and modern technology, the study of flow and heat transfer in porous media exposed to non-Newtonian and Newtonian fluid flows has gotten a lot of attention [31–35].

By considering mathematical formulations, their solutions, and the motivations carried by the researchers reported above, we propose a new symmetry transformation for non-Newtonian thermally magnetized flow subject to both non-permeable and permeable sheets. The effort in design is explained in the various sections. In Section 1, the limited literature survey on mathematical formulation subject to fluid flow fields is reported. In Section 2, the flow formulation is disclosed. The procedure to obtain a scaling transformation is debated in Section 3. Section 4 is devoted to sharing the procedure adopted for numerical solutions. The observations are debated in Section 5 with the parallel graphical outcomes. The important results are itemized in Section 6. We conclude that the new scaling group of transformations will help researchers implement such exercise on their problems for batter narration of flow problems by using symmetry analysis with mathematical modeling.

2. Flow Formulation

The flow of Williamson fluid (WF) is considered over a heated flat surface. The surface was taken as porous, and an external magnetic field was applied perpendicular to the flow. The heat transfer in fluid with heat source/sink effect was entertained, and concentration aspects of fluid were taken in the presence of a first-order chemical reaction. At the surface, both temperature and velocity slip effects were also assumed. The physical model of the flow problem is given in Figure 1. The present physical model was studied by using the continuity equation, Cauchy momentum equation, energy equation, and concentration equation. The said ultimate equations are:

$$\begin{aligned} \tfrac{\partial \rho}{\partial t} + \nabla \cdot (\rho \widetilde{V}), \\ \rho \tfrac{d\widetilde{V}}{dt} = \nabla \cdot \overleftrightarrow{T} + \widetilde{d}, \\ \tfrac{\partial \widetilde{T}}{\partial t} + \widetilde{V}.\nabla \widetilde{T} = \tfrac{k}{\rho c_p} \nabla^2 \widetilde{T}, \\ \tfrac{\partial \widetilde{C}}{\partial t} + \widetilde{V}.\nabla \widetilde{C} = D_c \nabla^2 \widetilde{C}. \end{aligned} \tag{1}$$

To obtain a system of differentials for our problem, we needed the particular rheology of the Williamson fluid model [36], which could be assessed using the following constitutive relation for the Williamson fluid model:

$$\overleftrightarrow{T} = -p \overleftrightarrow{I} + \overleftrightarrow{\tau} \left(= \mu_\infty + \frac{\mu_0 - \mu_\infty}{1 - \Gamma \dot{\Omega}} \right) \Delta_1, \tag{2}$$

where $\dot{\Omega}$ is given as:

$$\dot{\Omega} = \sqrt{\frac{\sum_i \sum_j \dot{\Omega}_{ij} \dot{\Omega}_{ji}}{2}} = \sqrt{\frac{\varpi}{2}}, \text{ with } \varpi = \frac{\text{trace}\left[\Delta_1\right]^2}{2}. \tag{3}$$

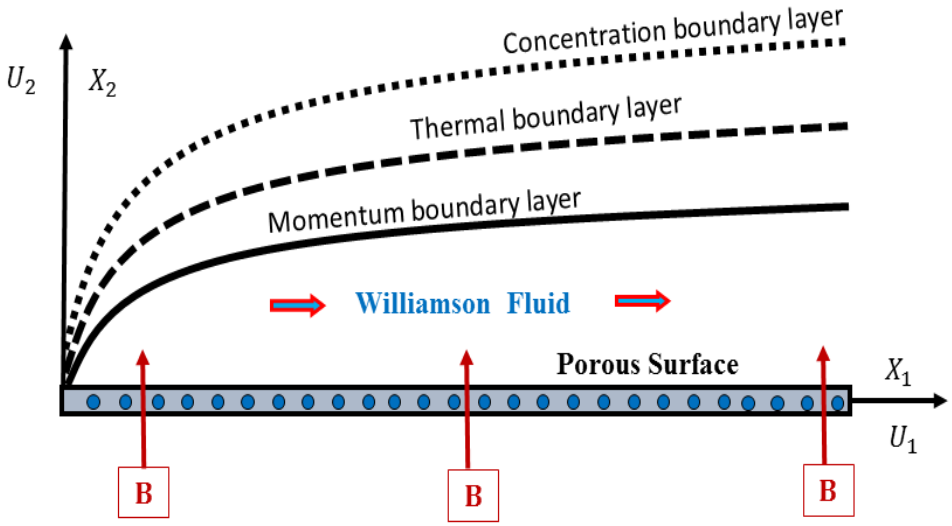

Figure 1. Description of flow.

For the present problem we considered $\mu_\infty = 0$ and $\Gamma\dot{\Omega} < 1$. Hence, Equation (2) gives:

$$\overleftrightarrow{T} = -p\overleftrightarrow{I} + \overleftrightarrow{\tau}\left(= \frac{\mu_0}{1-\Gamma\dot{\Omega}}\right)\Delta_1, \tag{4}$$

Carrying the binomial expansion in Equation (3), we get:

$$\overleftrightarrow{T} \cong -p\overleftrightarrow{I} + \mu_0\left(1+\Gamma\dot{\Omega}\right)\Delta_1. \tag{5}$$

The Williamson fluid velocity U_1 is taken along the X_1-axis and U_2 is towards X_2-axis. Further, by considering assumptions of steady flow, the external magnetic field effect, heat sink/source effect, chemical reaction effect, and using the Williamson fluid constitutive relation (Equation (5)) into Equation (1), resulted in the following coupled non-linear flow narrating differential equations for our physical problem:

$$\frac{\partial U_1}{\partial X_1} + \frac{\partial U_2}{\partial X_2}, \tag{6}$$

$$U_1\left(\frac{\partial U_1}{\partial X_1}\right) + U_2\left(\frac{\partial U_1}{\partial X_2}\right) = \nu_1\left(\frac{\partial^2 U_1}{\partial {X_2}^2}\right) + \sqrt{2}\,\nu_1\Gamma\left(\frac{\partial U_1}{\partial X_2}\right)\left(\frac{\partial^2 U_1}{\partial {X_2}^2}\right) - \left(\frac{\sigma B^2}{\rho}\right)U_1 - \left(\frac{\mu}{\rho K_p}\right)U_1, \tag{7}$$

$$U_1\left(\frac{\partial \widetilde{T}}{\partial X_1}\right) + U_2\left(\frac{\partial \widetilde{T}}{\partial X_2}\right) = \frac{k}{c_p\rho}\left(\frac{\partial^2 \widetilde{T}}{\partial {X_2}^2}\right) + \left(\frac{Q_1}{c_p\rho}\right)\left(\widetilde{T} - \widetilde{T}_\infty\right), \tag{8}$$

$$U_1\left(\frac{\partial \widetilde{C}}{\partial X_1}\right) + U_2\left(\frac{\partial \widetilde{C}}{\partial X_2}\right) = D_c\left(\frac{\partial^2 \widetilde{C}}{\partial {X_2}^2}\right) - k_1\left(\widetilde{C} - \widetilde{C}_\infty\right), \tag{9}$$

along with boundary constraints:

$$\begin{aligned} &\widetilde{C} = \widetilde{C}_w,\ \widetilde{T} = \widetilde{T}_w + D_1\tfrac{\partial \widetilde{T}}{\partial X_2},\ U_2 = 0,\ U_1 = bX_1 + L_1\tfrac{\partial U_1}{\partial X_2},\ \text{with } X_2 = 0,\\ &\widetilde{C} \to \widetilde{C}_\infty,\ \widetilde{T} \to \widetilde{T}_\infty,\ U_1 \to 0,\ \text{for } X_2 \to \infty. \end{aligned} \tag{10}$$

Further, we used:

$$T = \frac{\widetilde{T} - \widetilde{T}_\infty}{\widetilde{T}_w - \widetilde{T}_\infty},\ C = \frac{\widetilde{C} - \widetilde{C}_\infty}{\widetilde{C}_w - \widetilde{C}_\infty},\ V = \frac{U_2}{\sqrt{b\nu_1}},\ U = \frac{U_1}{\sqrt{b\nu_1}},\ Y = \sqrt{\frac{b}{\nu_1}}\,X_2,\ X = \sqrt{\frac{b}{\nu_1}}\,X_1, \tag{11}$$

and obtained:

$$\frac{\partial U}{\partial X} + \frac{\partial V}{\partial Y} = 0, \tag{12}$$

$$U\left(\frac{\partial U}{\partial X}\right) + V\left(\frac{\partial U}{\partial Y}\right) = \sqrt{2}\, b\, \Gamma\left(\frac{\partial U}{\partial Y}\right)\left(\frac{\partial^2 U}{\partial Y^2}\right) + \frac{\partial^2 U}{\partial Y^2} - \left(\frac{\sigma B^2}{\rho\, b}\right)U - \left(\frac{\mu}{\rho\, b K_p}\right)U, \tag{13}$$

$$U\left(\frac{\partial T}{\partial X}\right) + V\left(\frac{\partial T}{\partial Y}\right) = \frac{k}{c_p \mu}\left(\frac{\partial^2 T}{\partial Y^2}\right) + \left(\frac{Q_1}{c_p \rho\, b}\right)T, \tag{14}$$

$$U\left(\frac{\partial C}{\partial X}\right) + V\left(\frac{\partial C}{\partial Y}\right) = \frac{D_c}{\nu_1}\left(\frac{\partial^2 C}{\partial Y^2}\right) - \frac{k_1}{b}C, \tag{15}$$

while the corresponding equations are:

$$\begin{aligned} &C = 1,\ T = 1 + \left(\sqrt{\tfrac{b}{\nu_1}}D_1\right)\tfrac{\partial T}{\partial Y},\ V = 0,\ U = X + \left(\sqrt{\tfrac{b}{\nu_1}}L_1\right)\tfrac{\partial U}{\partial Y},\ \text{for } Y = 0, \\ &C \to 0,\ T \to 0,\ Y \to 0,\ \text{for } Y \to \infty. \end{aligned} \tag{16}$$

The partial differential Equations (12) to (15) form a structure. These equations are strongly non-linear and coupled. So far, finding an exact solution was not possible. Therefore, we reduced the independent variables by using single parameter transformations for examination. Rather than continuing with transformations accessible in the literature, we found some specifically for the current problem. We needed the stream function relation:

$$U = \Psi_Y,\ V = -\Psi_X, \tag{17}$$

Equations (12)–(16) under Equation (17) gets the forms:

$$\frac{\partial^2 \Psi}{\partial X Y} - \frac{\partial^2 \Psi}{\partial Y X} = 0, \tag{18}$$

$$\begin{aligned} &\tfrac{\partial \Psi}{\partial Y}\left(\tfrac{\partial^2 \Psi}{\partial X Y}\right) - \tfrac{\partial \Psi}{\partial X}\left(\tfrac{\partial^2 \Psi}{\partial^2 Y}\right) = \tfrac{\partial^3 \Psi}{\partial^3 Y} + \sqrt{2}\, b\, \Gamma\left(\tfrac{\partial^2 \Psi}{\partial^2 Y}\right)\left(\tfrac{\partial^3 \Psi}{\partial^3 Y}\right) \\ &-\left(\tfrac{\sigma B^2}{\rho\, b} + \tfrac{\mu}{\rho b K_p}\right)\tfrac{\partial \Psi}{\partial Y}, \end{aligned} \tag{19}$$

$$\frac{\partial \Psi}{\partial Y}\left(\frac{\partial T}{\partial X}\right) - \frac{\partial \Psi}{\partial X}\left(\frac{\partial T}{\partial Y}\right) = \frac{k}{c_p \mu}\left(\frac{\partial^2 T}{\partial^2 Y}\right) + \left(\frac{Q_1}{c_p \rho\, b}\right)T, \tag{20}$$

$$\frac{\partial \Psi}{\partial Y}\left(\frac{\partial C}{\partial X}\right) - \frac{\partial \Psi}{\partial X}\left(\frac{\partial C}{\partial Y}\right) = \frac{D_c}{\nu_1}\left(\frac{\partial^2 C}{\partial^2 Y}\right) - \left(\frac{k_1}{b}\right)C, \tag{21}$$

the concerned endpoint conditions are:

$$\begin{aligned} &C = 1,\ T = 1 + \left(\sqrt{\tfrac{b}{\nu_1}}D_1\right)\tfrac{\partial T}{\partial Y},\ \tfrac{\partial \Psi}{\partial Y} = X + \left(\sqrt{\tfrac{b}{\nu_1}}L_1\right)\tfrac{\partial^2 \Psi}{\partial Y^2},\ \tfrac{\partial \Psi}{\partial X} = 0,\ \text{for } Y = 0, \\ &C \to 0,\ T \to 0,\ \tfrac{\partial \Psi}{\partial Y} \to 0,\ \to 0,\ \text{for } Y \to \infty. \end{aligned} \tag{22}$$

3. Symmetry Exploration

The Equations (6)–(9) are a series of partial differential equations that are strongly non-linear and coupled. Our aim was to decompose the equations into independent variables. For this, we needed a series of scaling transformations. As a result, the following one-parameter transformation category can be considered:

$$G_s:\ C^* = Ce^{\varepsilon \lambda_6},\ \Gamma^* = \Gamma e^{\varepsilon \lambda_5},\ T^* = Te^{\varepsilon \lambda_4},\ \Psi^* = \Psi e^{\varepsilon \lambda_3},\ Y_1 = Y\, e^{\varepsilon \lambda_2},\ X_1 = X\, e^{\varepsilon \lambda_1}, \tag{23}$$

here, the old coordinates $(C,\ T,\ \Gamma,\ \Psi,\ Y,\ X)$ were replaced with $(C^*,\ T^*,\ \Gamma^*,\ \Psi^*,\ Y_1,\ X_1)$ due to Equation (23). In this case, the implementation results in:

$$\begin{aligned} &e^{\varepsilon\,(\lambda_1+2\lambda_2-2\lambda_3)}\left(\frac{\partial\Psi^*}{\partial Y_1}\frac{\partial^2\Psi^*}{\partial X_1\partial Y_1}-\frac{\partial\Psi^*}{\partial X_1}\frac{\partial^2\Psi^*}{\partial {Y_1}^2}\right)=e^{\varepsilon\,(3\lambda_2-\lambda_3)}\left(\frac{\partial^3\Psi^*}{\partial {Y_1}^3}\right)\\ &+e^{\varepsilon\,(7\lambda_2-3\lambda_3-2\lambda_5)}\sqrt{2}\,b\,\Gamma^*\left(\frac{\partial^2\Psi^*}{\partial {Y_1}^2}\frac{\partial^3\Psi^*}{\partial {Y_1}^3}\right)-e^{\varepsilon\,(\lambda_2-\lambda_3)}\left(\frac{\sigma B^2}{\rho\,b}+\frac{\mu}{\rho b K_p}\right)\left(\frac{\partial\Psi^*}{\partial Y_1}\right), \end{aligned} \tag{24}$$

$$e^{\varepsilon\,(\lambda_1+\lambda_2-\lambda_3-\lambda_4)}\left(\frac{\partial\Psi^*}{\partial Y_1}\frac{\partial T^*}{\partial X_1}-\frac{\partial\Psi^*}{\partial X_1}\frac{\partial T^*}{\partial Y_1}\right)=e^{\varepsilon\,(2\lambda_2-\lambda_4)}\frac{k}{c_p\mu}\left(\frac{\partial^2\theta^*}{\partial {Y_1}^2}\right)+e^{-\varepsilon\,\lambda_4}\left(\frac{Q_1}{c_p\rho\,b}\right)T^*, \tag{25}$$

$$e^{\varepsilon\,(\lambda_1+\lambda_2-\lambda_3-\lambda_6)}\left(\frac{\partial\Psi^*}{\partial Y_1}\frac{\partial C^*}{\partial X_1}-\frac{\partial\Psi^*}{\partial X_1}\frac{\partial C^*}{\partial Y_1}\right)=\ e^{\varepsilon\,(2\lambda_2-\lambda_6)}\frac{D_c}{\nu_1}\left(\frac{\partial^2 C^*}{\partial {Y_1}^2}\right)-e^{-\varepsilon\,\lambda_6}\frac{k_1}{b}C^*, \tag{26}$$

carrying invariant condition for Equations (24)–(26) under G_s, we get:

$$\begin{aligned} &\lambda_1+2\lambda_2-2\lambda_3=3\lambda_2-\lambda_3=7\lambda_2-3\lambda_3-2\lambda_5=\lambda_2-\lambda_3,\\ &\lambda_1+\lambda_2-\lambda_3-\lambda_4=2\lambda_2-\lambda_4=-\lambda_4,\\ &\lambda_1+\lambda_2-\lambda_3-\lambda_6=2\lambda_2-\lambda_6=-\lambda_6, \end{aligned} \tag{27}$$

further (boundary conditions) BCs give $\lambda_4=0,$ and $\lambda_6=0$. Equation (27) results in:

$$\lambda_1=\lambda_1,\ \lambda_2=0,\ \lambda_3=\lambda_1,\ \lambda_4=0,\ \lambda_5=-\lambda_1 \text{ and } \lambda_6=0. \tag{28}$$

Equation (23) under Equation (28) offers:

$$G_s\ :\ C^*=C,\ \Gamma^*=\Gamma e^{-\varepsilon\,\lambda_1},\ T^*=T,\ \Psi^*=\Psi e^{\varepsilon\,\lambda_1},\ Y_1=Y\,,\ X_1=X\,e^{\varepsilon\,\lambda_1}. \tag{29}$$

Equation (29) with the use of Taylor's expansion around $\varepsilon=0$ up-to $O(\varepsilon)$, we get:

$$\begin{aligned} &G_s\ :\ C^*-C\approx 0+\ O(\varepsilon),\ \Gamma^*-\Gamma\approx -X\varepsilon\lambda_1+O(\varepsilon),\ T^*-T\approx 0+\ O(\varepsilon),\\ &\Psi^*-\Psi\approx X\varepsilon\lambda_1+O(\varepsilon),\ \ Y_1-Y\approx 0+\ O(\varepsilon),\ \ X_1-X\approx X\varepsilon\lambda_1+O(\varepsilon). \end{aligned} \tag{30}$$

Therefore, we have:

$$\frac{dC}{0}=\frac{d\Gamma}{-\lambda_1 X}=\frac{dT}{0}=\frac{dX}{\lambda_1 X}=\frac{d\Psi}{\lambda_1 X}=\frac{dY}{0}. \tag{31}$$

The use of Equation (31) results in:

$$C=C_w(\lambda),\ \Gamma=X^{-1}\Gamma_0,\ T=T_w(\lambda),\ \Psi=X\,F_w(\lambda),\ \ \lambda=Y, \tag{32}$$

Equations (19)–(22) under Equation (32) gives:

$$\begin{aligned} &\tfrac{d^3F_w(\lambda)}{d\lambda^3}-\left(\tfrac{dF_w(\lambda)}{d\lambda}\right)^2+\tfrac{d^2F_w(\lambda)}{d\lambda^2}F_w(\lambda)+Wb\tfrac{d^3F_w(\lambda)}{d\lambda^3}\left(\tfrac{d^2F_w(\lambda)}{d\lambda^2}\right)^2\\ &-Mg^2\tfrac{dF_w(\lambda)}{d\lambda}-Pm\tfrac{dF_w(\lambda)}{d\lambda}=0, \end{aligned} \tag{33}$$

$$\frac{d^2T_w(\lambda)}{d\lambda^2}+\mathrm{Pr}\left(F_w(\lambda)\frac{dT_w(\lambda)}{d\lambda}\right)+\mathrm{Pr}HsT_w(\lambda)=0, \tag{34}$$

$$\frac{d^2C_w(\lambda)}{d\lambda^2}+Sc\left(F_w(\lambda)\frac{dC_w(\lambda)}{d\eta}\right)-ScRsC_w(\lambda)=0, \tag{35}$$

while the reduced endpoint conditions are:

$$\begin{aligned} &C_w(\lambda) = 1,\ T_w(\lambda) = 1 + Ts\frac{dT_w(\lambda)}{d\lambda},\\ &F_w(\lambda) = 0,\ \frac{dF_w(\lambda)}{d\lambda} = 1 + Vp\frac{d^2F_w(\lambda)}{d\lambda^2},\ at\ \lambda = 0,\\ &C_w(\lambda) \to 0,\ T_w(\lambda) \to 0,\ \frac{dF_w(\lambda)}{d\lambda} \to 0,\ \text{when } \lambda \to \infty. \end{aligned} \tag{36}$$

The Williamson fluid fills a semi-infinite domain. As a result, the Sherwood number (ShD), Skin Friction Coefficient (Skin-FC), and Nusselt number (Nm) are among the surface quantities. These surface quantities have the following mathematical expression:

$$\begin{aligned} &C_F = \frac{\overleftrightarrow{\tau}_w}{\rho\,(bX)^2},\ NU_X = \frac{X\,q_w}{k(\widetilde{T}_w - \widetilde{T}_\infty)},\ ShU_X = \frac{X q_m}{D_c(\widetilde{C}_w - \widetilde{C}_\infty)},\\ &\overleftrightarrow{\tau}_w = \frac{\partial U}{\partial Y} + \frac{\Gamma}{\sqrt{2}}\left(\frac{\partial U}{\partial Y}\right),\ q_w = -k\,\widetilde{T}_Y,\ q_m = -D_c\widetilde{C}_Y, \end{aligned} \tag{37}$$

the corresponding dimensionless forms can be written as:

$$\sqrt{\mathrm{Re}}C_F = \frac{d^2F_w(0)}{d\lambda^2} + \frac{Wb}{2}\left(\frac{d^2F_w(0)}{d\lambda^2}\right)^2,\ \frac{NU_X}{\sqrt{\mathrm{Re}}} = -\frac{dT_w(0)}{d\lambda},\ \frac{ShU_X}{\sqrt{\mathrm{Re}}} = -\frac{dC_w(0)}{d\lambda}. \tag{38}$$

and the flow parameters are given as:

$$\begin{aligned} &Wb = \sqrt{2}\Gamma_0\,b,\ Mg = \sqrt{\frac{\sigma B^2}{\rho b}},\ \mathrm{Pr} = \frac{\mu c_p}{\kappa},\ Hr = \frac{Q_1}{\rho c_p b},\\ &Sc = \frac{\nu_1}{D_c},\ Vp = \sqrt{\frac{b}{\nu_1}}L_1,\ Ts = \sqrt{\frac{b}{\nu_1}}D_1,\ Pm = \frac{\nu}{bK_p},\ Rs = \frac{k_1}{b}. \end{aligned} \tag{39}$$

where *Wb*, *Mg*, *Pr*, *Hr*, *Sc*, *Vp*, *Ts*, *Pm*, and *Rs* denote the Wessinberg number, magnetic field parameter, Prandtl number, heat generation parameter, Schmidt number, velocity slip parameter, thermal slip parameter, porosity parameter, and chemical reaction parameter, respectively.

4. Solution Procedure

We took into account the Williamson fluid flow towards a stretched porous surface in this paper. In the existence of heat absorption, heat generation, and chemically reactive species, the slip flow field was thermally magnetized. The assumptions are mathematically represented as PDEs. The use of a Williamson fluid with many physical special effects resulted in highly non-linear PDEs, making an exact solution unattainable at this time. When an exact answer appears to be impossible, we always look for a numerical solution [37,38]. Researchers in this subject, in particular, used a variety of approaches to report numerical solutions. The majority of methods for investigators seeking a numerical solution are by transforming the PDEs into ODEs, which are then solved by the numerical scheme. It is worth noting that the conversion from PDEs to ODEs is accomplished through a specific set of transformations [39,40]. Many scholars consider such transformations straight from the literature rather than obtaining specific transformations of the flow problem. This does not allow for a better narration of the flow fields. In our situation, we used symmetry analysis to provide transformations for equations. We created coupled ODEs using these transformations and solved them using a shooting method combined with the RK arrangement. It is worth noting that we employed self-coding to implement the shooting approach by converting Equations (33)–(36) into an initial value problem. The reduced initial value problem was then transformed into a system of seven first-order differential equations, which were solved by selecting three missing conditions as appropriate starting estimates. The computed solution converges if the boundary residuals are less than the tolerance error 10^{-6}. If the calculated results do not meet this criterion, the starting estimates are adjusted using Newton's method, and the operation is repeated until the solution meets the chosen

convergence threshold. Further, ShD, Nm, Skin-FC, WF concentration, WF velocity, and WF temperature are considered as the quantities of interest. Here, we have eight differential flow variables, namely *Wb*, *Vp*, *Mg*, *Pm*, *Ts*, *Hs*, *Pr*, and *Hr*. The effects of such flow variables are inspected on WF temperature, WF velocity, WF concentration, Skin-FC, Nm, and ShD. The range of flow variables was chosen in such a way that the method's convergence and stability are maintained. The final observations in this direction are shared by using line graphs and tables. The ShD, Nm, and Skin-FC were the surface quantities of concern. These quantities were estimated by taking into account a variety of physical frames. The variation in Skin-FC for non-slip and slip flows is shown in Table 1 with positive Wb values. When *Wb* = 0.1, 0.2, 0.3, and 0.4 were increased for *Vp* = 0, the Skin-FC decreased intensely. Furthermore, the Skin-FC was found to be a diminishing function of *Wb* when *Vp* = 0.5. For iteration in porosity parameter, Table 2 provides the Skin-FC outcomes for both magnetic and non-magnetized cases. When *Mg* = 0, the Skin-FC was found to be rising as a function of *Pm* in an absolute sense. Furthermore, when *Pm* = 0.1, 0.2, 0.3, and 0.4 were increased for Mg = 0.5, the Skin-FC displayed inciting values. The Skin-FC was found to be an increasing function of *Pm* for both fields. Skin-FC numerical values for non-permeable and permeable sheets are listed in Table 3. In this scenario, we looked at the magnetized flow on a case-by-case basis, namely permeable surface (*Pm* = 0) and non-permeable surface (*Pm* = 0.5). When we increased *Wb* = 0.1, 0.2, 0.3, and 0.4 for *Pm* = 0, the Skin-FC decreased considerably. Furthermore, at *Pm* = 0.5, Skin-FC was found to be a decreasing function of Wm. Physically, the resistance encountered by particles decreased as *Wb* grew.

Table 1. Skin-FC variation towards *Wb* in slip and non-slip flows.

Wb	$F''_w(0)$		**Skin-FC**	
	***Vp* = 0.5**	***Vp* = 0.0**	***Vp* = 0.5**	***Vp* = 0.0**
0.1	−1.0926	−0.8324	−1.0329	−0.7978
0.2	−1.1401	−0.8522	−1.0101	−0.7796
0.3	−1.2016	−0.8749	−0.9850	−0.7601
0.4	−1.2887	−0.9017	−0.9566	−0.7391

Table 2. Skin-FC variation towards *Pm* in magnetic and non-magnetic fields.

Pm	$F''_w(0)$		**Skin-FC**	
	***Mg* = 0.0**	***Mg* = 0.5**	***Mg* = 0.0**	***Mg* = 0.5**
0.1	−0.9378	−0.9543	−0.8938	−0.9088
0.2	−0.9784	−0.9942	−0.9305	−0.9448
0.3	−1.0172	−1.0323	−0.9655	−0.9790
0.4	−1.0544	−1.0688	−0.9988	−1.0117

Table 3. Skin-FC variation towards *Wb* in porous and non-porous mediums.

Wb	$F''_w(0)$		**Skin-FC**	
	***Pm* = 0.0**	***Pm* = 0.5**	***Pm* = 0.0**	***Pm* = 0.5**
0.1	−0.8994	−0.9824	−0.8590	−0.9341
0.2	−0.9258	−1.0146	−0.8401	−0.9117
0.3	−0.9570	−1.0536	−0.8196	−0.8871
0.4	−0.9954	−1.1031	−0.7972	−0.8597

5. Results Analysis

The WF was fitted above the permeable magnetized surface. In the existence of heat generation and absorption special effects, the thermal flow regime was carried out. Velocity and thermal slip were also taken into account. Consideration of the concentration equation, as well as the chemical reaction, adds to the novelty. The problem was investigated numerically. In detail, the impact of *Pm*, *Mg*, *Vp*, and *Wb* were investigated on WF velocity and shown with the help of Figures 2–5, respectively. In detail, the effect of *Pm* = 0.0, 0.3, 0.6 on WF velocity was investigated, and observations in this way are shown in Figure 2. It is worth noting that when *Pm* = 0.0, the fluid flow is across a non-permeable surface, and the velocity strength of WF is much higher than when *Pm* = 0.3 and *Pm* = 0.6. Overall, it is seen that velocity declines as *Pm* increases. The porosity parameter possesses an inverse relation towards permeability of the porous medium; therefore, increases in the porosity parameter cause a decline in the stretching rate of the flat surface. Since we considered the no-slip condition, a reduction in stretching rate resulted in lower values of the velocity of WF. Figure 3 offers the variations *Mg* = 0.0, 0.5, and 0.9, which are all positive values. Here, *Mg* = 0.0 denotes the absence of a magnetic field, and velocity has a large value because there is no Lorentz force. The WF velocity is retarded for *Mg* = 0.5 and *Mg* = 0.9 as compared to *Mg* = 0.0. When *Mg* = 0.9 was compared to *Mg* = 0.0 and 0.5, the fall in WF velocity magnitude was greater. It has been noticed that as *Mg* is increased, the WF velocity decreases. One should note that the non-zero value of the magnetic field parameter gives birth to Lorentz forces. Here, we simulated *Mg* = 0.0, 0.5, and 0.9. The positive values 0.5 and 0.9 enhance the strength of the Lorentz force, and due to the resistive nature of the Lorentz force, the WF particles met higher resistance; this led to a decline in WF velocity. For *Vp* = 0.0, 0.2, and 0.4, the velocity distributions subject to the permeable magnetic surface are shown in Figure 4. We established non-slip Williamson fluid flow with *Vp* = 0, and the WF velocity magnitude was larger than with *Vp* = 0.2 and 0.4. We discovered that WF velocity over a magnetic surface decreased as *Vp* increased. Variations in *Wb* = 0.1, 0.3, and 0.7 are shown in Figure 5 as a line graph of WF velocity. WF velocity has an inverse relationship with positive Wb values, as shown in the graph. It is worth mentioning that raising *Wb* reduces WF velocity, and the drop is of average scale. Positive values of *Wb* increased the Williamson fluid relaxation time. The higher relaxation time increased the viscosity of fluid due to which fluid flow faced higher resistance, and as a result, the WF declined.

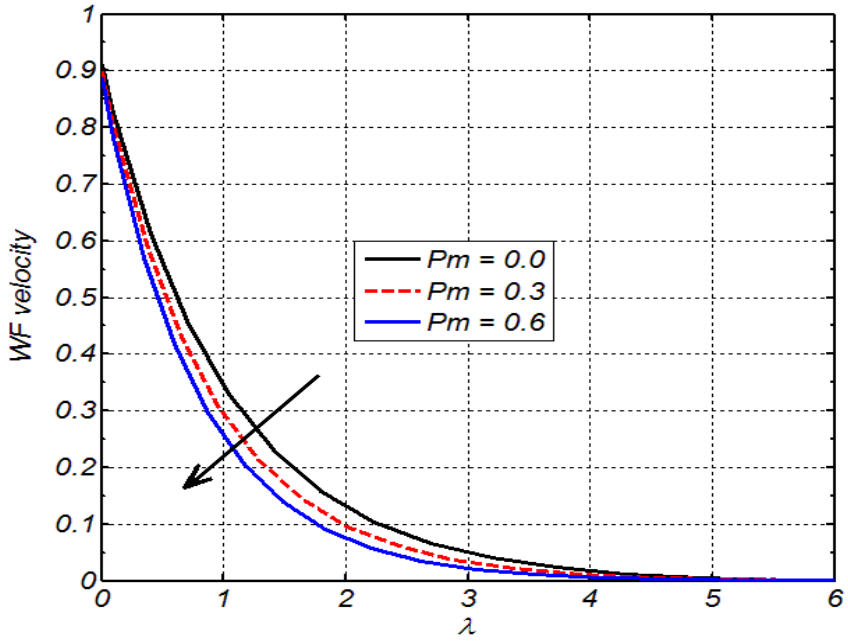

Figure 2. *Pm* versus WF velocity.

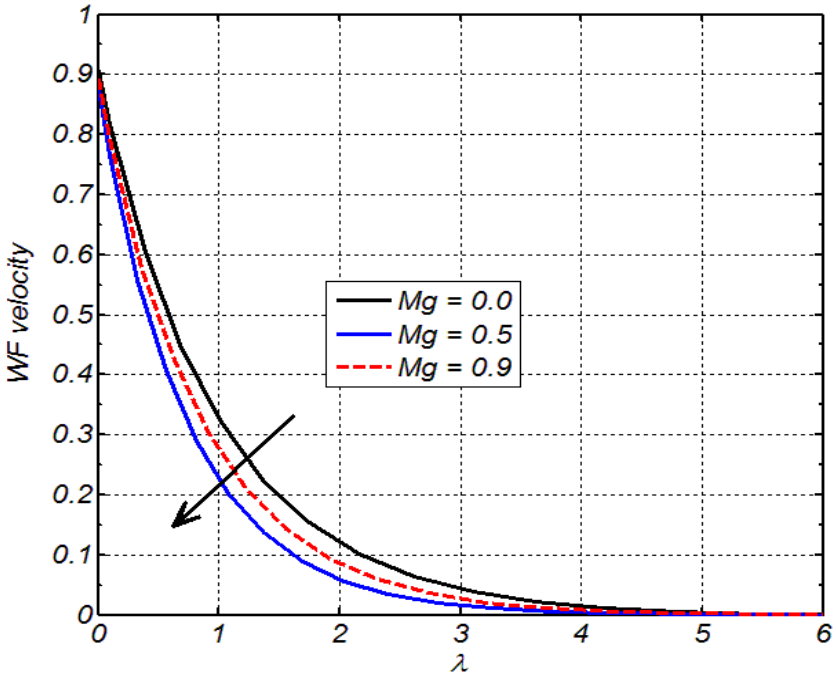

Figure 3. *Mg* versus WF velocity.

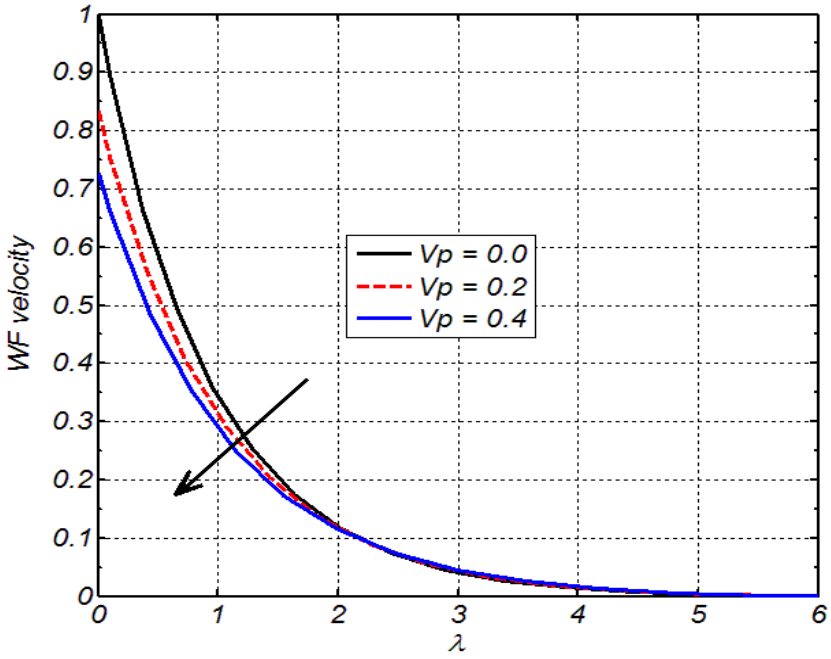

Figure 4. *Vp* versus WF velocity.

For both magnetized and non-magnetized situations, Table 4 was used to calculate the Skin-FC changes towards *Wb*. To begin, we assumed that the WF fluid was positioned above a non-magnetic (*Mg* = 0) permeable surface. When *Mg* was set to 0, we saw a drop in Skin-FC in absolute terms as *Wb* was increased. For magnetized WF flow across a stretched surface, the Skin-FC was also determined. Therefore, for Mg = 0.5, we discovered that Skin-FC decreased the function of *Wb*. In terms of physics, Skin-FC implied that the surface exerts an opposing drag force on fluid particles. As a result, increasing *Wb* = 0.1, 0.2, 0.3, 0.4 reduced the resistance faced by particles in both frames. Skin-FC numerical values for non-permeable and permeable sheets are presented in Table 5 for *Mg* = 0.1, 0.2, 0.3, and 0.4, respectively. Table 5 shows that in both non-magnetic and magnetized fields, the resistance

provided by the surface increased as *Mg* values increased. Table 6 shows Nm variations for both magnetic and non-magnetized frames as they approach greater Pr values. When Pr = 1.1, 1.2, 1.3, and 1.4 were increased for *Mg* = 0, which is the non-magnetized condition, the Nm increased considerably. Similarly, when *Mg* = 0.5, Nm rose in response to greater Pr values.

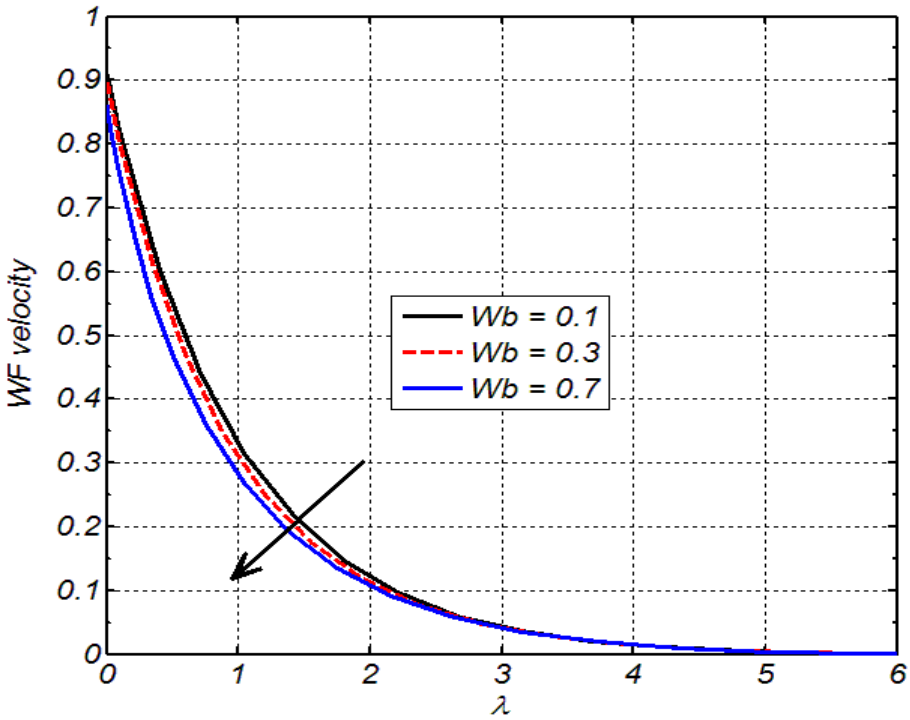

Figure 5. *Wb* versus WF velocity.

Table 4. Skin-FC variation towards *Wb* in magnetic and non-magnetic fields.

Wb	$F''_w(0)$		Skin-FC	
	***Mg* = 0.0**	***Mg* = 0.5**	***Mg* = 0.0**	***Mg* = 0.5**
0.1	−0.9378	−0.9543	−0.8938	−0.9088
0.2	−0.9668	−0.9844	−0.8733	−0.8875
0.3	−1.0015	−1.0207	−0.8510	−0.8644
0.4	−1.0447	−1.0662	−0.8264	−0.8388

Table 5. Skin-FC variation towards *Mg* in porous and non-porous mediums.

Mg	$F''_w(0)$		Skin-FC	
	***Pm* = 0.0**	***Pm* = 0.5**	***Pm* = 0.0**	***Pm* = 0.5**
0.1	−0.8994	−0.9824	−0.8590	−0.9341
0.2	−0.9124	−0.9942	−0.8708	−0.9448
0.3	−0.9336	−1.0134	−0.8900	−0.9621
0.4	−0.9624	−1.0397	−0.9161	−0.9857

The WF temperature dependency on *Pr*, *Hs*, *Ts*, and *Hr* was examined and offered in terms of line graphs, as shown in Figures 6–9, respectively. To be more specific, the influence of Pr on temperature is depicted in Figure 6.

Table 6. Nm variation towards Pr in magnetic and non-magnetic fields.

Pr	Nm	
	***Mg* = 0.0**	***Mg* = 0.5**
1.1	−0.4431	−0.4375
1.2	−0.4720	−0.4662
1.3	−0.5000	−0.4942
1.4	−0.5272	−0.5213

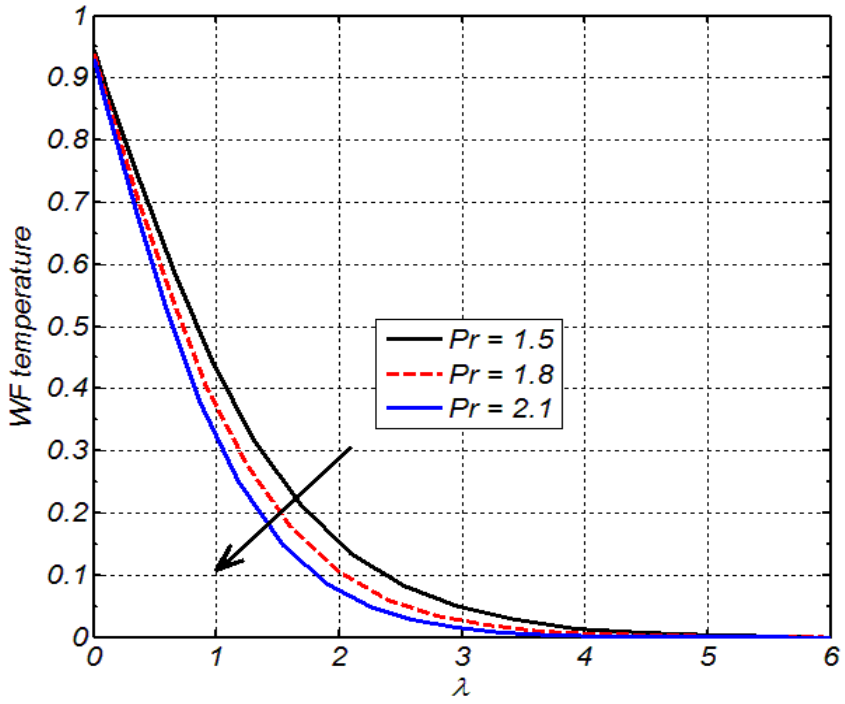

Figure 6. Pr versus WF temperature.

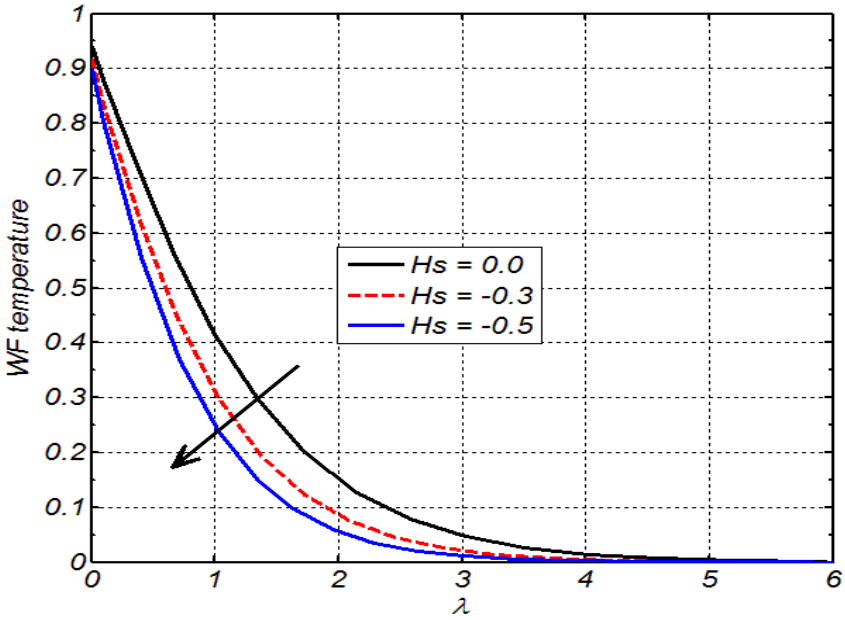

Figure 7. *Hs* versus WF temperature.

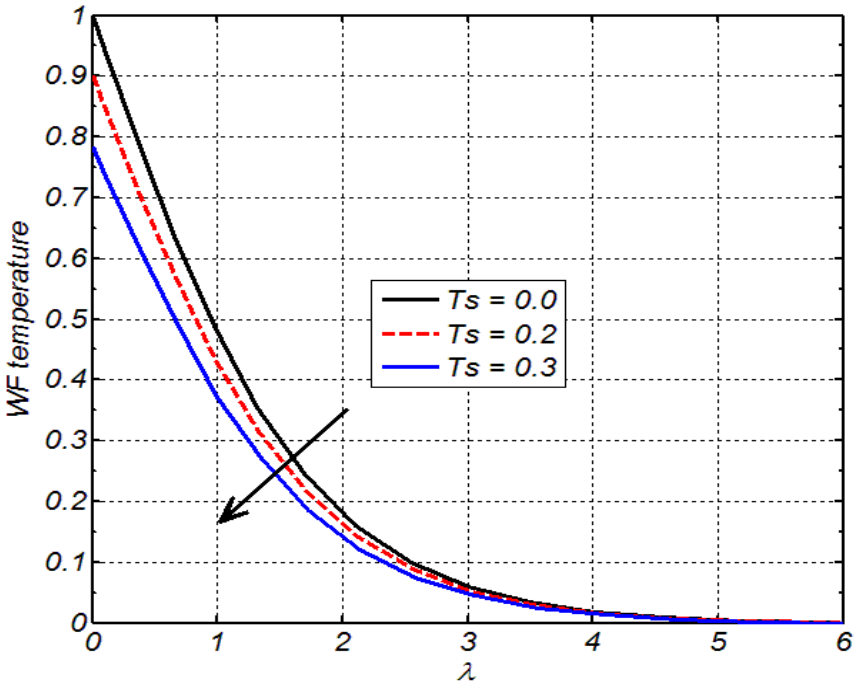

Figure 8. *Ts* versus WF temperature.

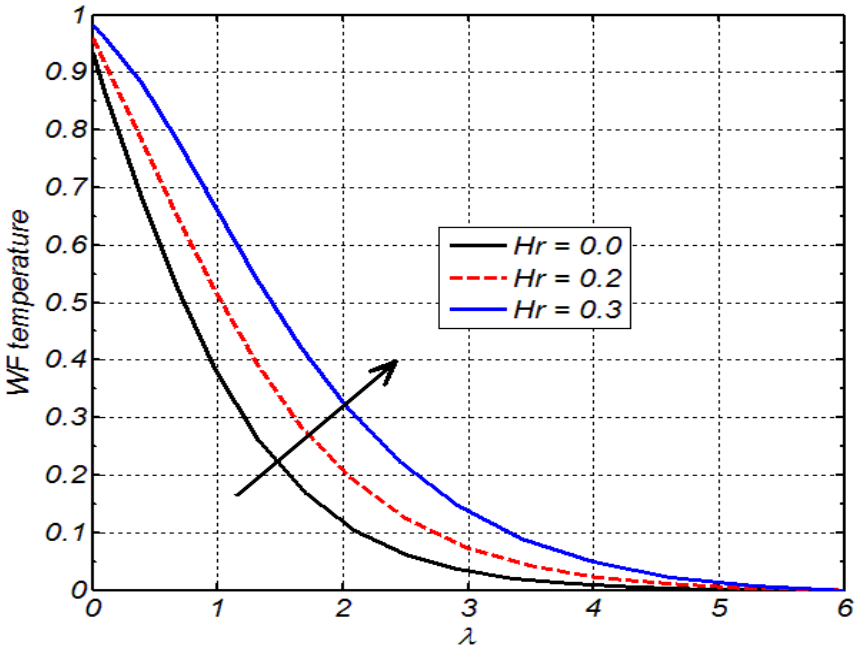

Figure 9. *Hr* versus WF temperature.

In this case, the positive variation in Pr = 1.5, 1.8, and 2.1 was taken into account. We have seen that when we have such a higher iteration, the temperature drops. Because Pr has an inverse relation with the fluid thermal diffusivity, we witnessed a decline in thermal diffusivity and, as a result, a considerable drop in WF temperature when we iterated Pr = 1.5, 1.8, and 2.1. The effect of *Hs* on WF temperature is depicted in Figure 7. WF temperature decreased when we iterated *Hs* = 0.0, −0.3, and −0.5. Iterations with *Hs* = 0.0, −0.3, and −0.5 caused energy loss and a drop in the overall temperature. The influence of the thermal slip parameter on WF temperature is offered in Figure 8. *Ts* = 0.0, 0.2, and 0.3 were employed in this line graph investigation. It is worth noting that we got a non-thermal case for *Ts* = 0.0. In this situation, the temperature appeared to be higher than *Ts* = 0.2

and *Ts* = 0.3. Overall, the WF temperature appeared to be falling as *Ts* increased. Figure 9 depicts the impact of heat generation on the thermal flow regime of a WF fluid towards a porous magnetic surface. The WF temperature increased dramatically when we iterated *Hr* = 0, 0.2, and 0.3. When *Hr* = 0.0, the thermal flow regime has no heat-producing impact, and the temperature of WF is smaller in magnitude than when *Hr* = 0.2 and 0.3 are utilized. This is because energy is generated inside the flow regime when we iterate the *Hr*, resulting in a rise in WF temperature. The impact of Sc and *Rs* is examined on WF concentration, see Figures 10 and 11. Particularly, Figure 10 deals with the impact of Sc on WF concentration. Sc was carried out in the following way; Sc = 1.8, 2.2, and 2.6. The WF concentration decreased as we iterated Sc. This effect was comparable to the Pr effect on WF temperature. As the Sc value increased, the mass diffusivity reduced, and the concentration of WF fell. The flow was considered with chemical reaction, and the resultant flow variable was the chemical reaction parameter *Rs*. In this direction we iterated *Rs* = 0.0, 0.2, and 0.4. It was found that for *Rs* = 0.0, the WF flow was non-reactive, and one can note that here, the concentration magnitude was higher as compared to *Rs* = 0.2 and *Rs* = 0.4. Together, the WF concentration showed declining values towards *Rs* = 0.0, 0.2, and 0.4.

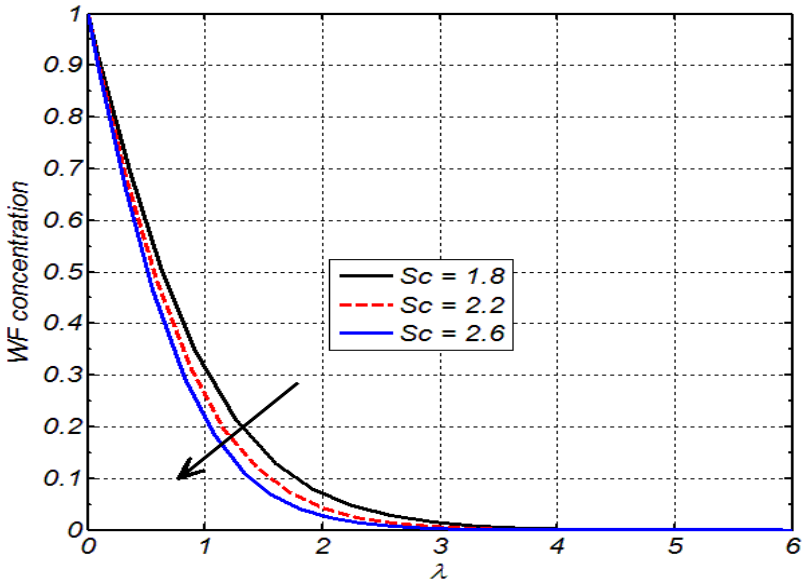

Figure 10. Sc versus WF concentration.

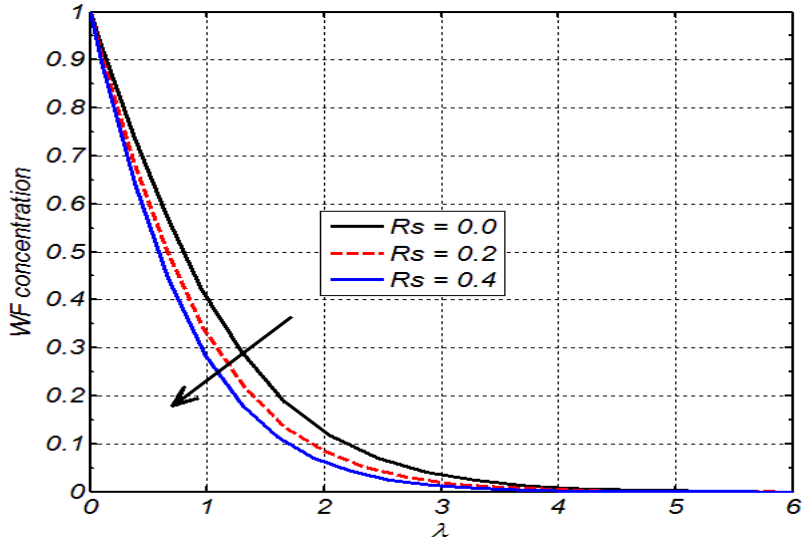

Figure 11. *Rs* versus WF concentration.

Tables 7 and 8 offer the Nusselt number outcomes for various parameters in different frames of reference. The Nm variations in thermal/non-thermal slip flows are reported in Table 7. For the non-thermal case (Ts = 0), we confirmed that when Pr = 1.1, 1.2, 1.3, and 1.4 increased, the Nm upturns. The Nm increased as Pr increased when Ts = 0.5. In thermal/non-thermal cases, the transfer of heat normal to the permeable surface was directly related to Pr. The transfer of heat normal to both permeable and non-permeable surfaces was apparent, see Table 8.

Table 7. Nm variation towards Pr in thermal and non-thermal flow fields.

Pr	Nm	
	Ts = 0.0	Ts = 0.5
1.1	−0.4974	−0.4524
1.2	−0.5313	−0.4803
1.3	−0.5644	−0.5071
1.4	−0.5965	−0.5329

Table 8. Nm variation towards Pr in porous and non-porous mediums.

Pr	Nm	
	Pm = 0.0	Pm = 0.5
1.1	−0.4860	−0.4621
1.2	−0.5169	−0.4926
1.3	−0.5467	−0.5222
1.4	−0.5754	−0.5508

We found that for both surfaces, the rate was an increasing function of Pr. Tables 9–11 were constructed to examine the variation in ShD towards three different frames, namely permeable and non-permeable surfaces, magnetic and non-magnetic fields, chemically reactive and non-reactive flows. The variation in ShD was observed for both non-permeable and permeable sheets (Table 9). The Pm = 0.0 implies the porous surface assumption, and for this case, we observed that when we increased Sc, the ShD increased reasonably. Together in both cases, porous and non-porous mediums, the ShD had a direct relation with Sc. Table 10 offers the ShD variation in both magnetic and non-magnetic fields towards Sc. We noticed that for both Mg = 0.0 and Mg = 0.5, the ShD showed inciting values towards Sc = 2.1, 2.2, 2.3, and 2.4. The impact of iteration in Sc on ShD for both chemically reactive and non-reactive flows was investigated and offered in terms of Table 11. In detail, Rs = 0.0 implies the case of non-reactive flow, and in this case, we noticed that ShD showed inciting values towards Sc = 2.1, 2.2, 2.3, and 2.4. Further, it can be seen that this impact was the same for chemically reactive flow. The magnitude of ShD variation was higher in the case of reactive flow.

Table 9. ShD variation towards Sc in porous and non-porous mediums.

Sc	ShD	
	Pm = 0.0	Pm = 0.5
2.1	−1.0029	−0.9816
2.2	−1.0305	−1.0090
2.3	−1.0576	−1.0358
2.4	−1.0840	−1.0621

Table 10. ShD variation towards Sc in magnetized and non-magnetized flow fields.

Sc	ShD	
	Mg = 0.0	Mg = 0.5
2.1	−0.9930	−0.9888
2.2	−1.0205	−1.0163
2.3	−1.0475	−1.0432
2.4	−1.0739	−1.0695

Table 11. ShD variation towards Sc in reactive and non-reactive flow fields.

Sc	ShD	
	Rs = 0.0	Rs = 0.5
2.1	−0.8771	−1.0947
2.2	−0.4374	−1.1239
2.3	−0.4484	−1.1526
2.4	−0.9530	−1.1806

6. Key Outcomes

The group-theoretic analysis was performed to determine the specific scaling transformations of the heat transfer problem, and through these specific transformations, we narrate the whole description of chemically reactive thermally magnetized Williamson fluid toward a stretched heated porous surface. Owing to the numerical solution, we arrived at the following conclusions:

- WF velocity had inverse relations with *Pm*, *Mg*, *Vp*, and *Wb*.
- WF temperature showed a declining nature with Ts, Pr, and Hs.
- Higher values of Hr resulted in inciting values of temperature.
- WF concentration was found with decreasing functions of Sc and *Rs*.
- Nm showed inciting values towards Pr for thermal no-slip and slip regimes.
- For magnetized and non-magnetized flows, ShD showed higher values of Sc.
- In both chemically reactive and non-reactive cases, ShD increased as Sc increased.
- Skin-FC showed declining values towards *Wb* in both non-magnetic and magnetic fields.
- Skin-FC at both non-permeable and permeable sheets showed a direct relation with *Mg*.

Author Contributions: Conceptualization, methodology, formal analysis; writing—original draft preparation, K.U.R.; visualization, validation, data curation, supervision, W.S.; project administration, validation, supervision, K.A.; Investigation, Writing—review and editing, T.A.M.S. All authors have read and agreed to the published version of the manuscript.

Funding: This research received no external funding.

Institutional Review Board Statement: Not applicable.

Informed Consent Statement: Not applicable.

Data Availability Statement: All data is available in manuscript.

Acknowledgments: The authors would like to thank Prince Sultan University, Saudi Arabia, for the technical support through the TAS research lab. Further, K.U. Rehman receives a postdoctoral fellowship under the supervision of Wasfi Shatanawi at TAS Lab.

Conflicts of Interest: The authors declare no conflict of interest.

Nomenclature

d/dt	Material time derivative
$\vec{d}$	Body force
$\overleftrightarrow{T}$	Cauchy stress tensor
p	Pressure
$\overleftrightarrow{I}$	Identity tensor
$\overleftrightarrow{\tau}$	Extra stress tensor for Williamson fluid model
μ_∞	Infinite shear rate-limiting viscosity
μ_0	Zero shear rate-limiting viscosity
Γ	Material time constant
Δ_1	First Rivilin-Erickson tensor
(X_1, X_2)	Space variables
$\widetilde{V} = (U_1, U_2)$	Velocity field
ν_1	Kinematic viscosity
B	Applied magnetic field strength
σ	Fluid electrical conductivity
ρ	Fluid density
μ	Dynamic viscosity
K_p	Permeability of the porous medium
$\widetilde{T}_\infty$	Ambient temperature
$\widetilde{T}$	Fluid temperature
Q_1	Heat generation/absorption coefficient
c_p	Specific heat at constant pressure
k	Thermal conductivity
$\widetilde{C}_\infty$	Ambient concentration
$\widetilde{C}$	Fluid concentration
D_c	Mass diffusivity
k_1	Chemical reaction rate
D_1	Thermal slip factor
L_1	Velocity slip factor
b	Stretching rate
$V = (U, V)$	Velocity field (dimensionless)
(X, Y)	Space variables (dimensionless)
Ψ	Stream function
ε	Small parameter
$\lambda_{i=1\ldots6}$	Real numbers
${F_m}'(\lambda)$	Dimensionless velocity
$T_w(\lambda)$	Dimensionless temperature
$C_w(\lambda)$	Dimensionless concentration
Pm	Porosity parameter
Mg	Magnetic field parameter
Wb	Weissenberg number
Hr	Heat generation parameter
Sc	Schmidt number
Pr	Prandtl number
Rs	Chemical reaction parameter
Ts	Thermal slip parameter
Vp	Velocity slip parameter
Hs	Heat absorption parameter
ShD = $-{C_w}'(0)$	Sherwood number
Nm = $-{T_w}'(0)$	Nusselt number
Skin-FC = $\sqrt{\mathrm{Re}}C_F$	Skin friction coefficient

References

1. Vajravelu, K.; Rollins, D. Heat transfer in a viscoelastic fluid over a stretching sheet. *J. Math. Anal. Appl.* **1991**, *158*, 241–255. [CrossRef]
2. Andersson, I.H.; Aarseth, J.B.; Dandapat, B.S. Heat transfer in a liquid film on an unsteady stretching surface. *Int. J. Heat Mass Transf.* **2000**, *43*, 69–74. [CrossRef]
3. Abel, M.S.; Khan, S.K.; Prasad, K.V. Study of viscoelastic fluid flow and heat transfer over a stretching sheet with variable viscosity. *Int. J. Non-Linear Mech.* **2002**, *37*, 81–88. [CrossRef]
4. Zakaria, M. Magnetohydrodynamic viscoelastic boundary layer flow past a stretching plate and heat transfer. *Appl. Math. Comput.* **2004**, *155*, 165–177. [CrossRef]
5. Cortell, R. A note on flow and heat transfer of a viscoelastic fluid over a stretching sheet. *Int. J. Non-Linear Mech.* **2006**, *41*, 78–85. [CrossRef]
6. Abel, M.S.; Mahesha, N. Heat transfer in MHD viscoelastic fluid flow over a stretching sheet with variable thermal conductivity, non-uniform heat source and radiation. *Appl. Math. Model.* **2008**, *32*, 1965–1983. [CrossRef]
7. Pal, D. Mixed convection heat transfer in the boundary layers on an exponentially stretching surface with magnetic field. *Appl. Math. Comput.* **2010**, *217*, 2356–2369. [CrossRef]
8. Ashrafi, N.; Mohamadali, M. Transient flow and heat transfer of pseudoplastic fluids on a stretching sheet. *Appl. Math. Comput.* **2014**, *228*, 153–161. [CrossRef]
9. Zhang, Y.; Zhang, M.; Bai, Y. Flow and heat transfer of an Oldroyd-B nanofluid thin film over an unsteady stretching sheet. *J. Mol. Liq.* **2016**, *220*, 665–670. [CrossRef]
10. Chen, X.; Ye, Y.; Zhang, X.; Zheng, L. Lie-group similarity solution and analysis for fractional viscoelastic MHD fluid over a stretching sheet. *Comput. Math. Appl.* **2018**, *75*, 3002–3011. [CrossRef]
11. Jusoh, R.; Nazar, R.; Pop, I. Magnetohydrodynamic rotating flow and heat transfer of ferrofluid due to an exponentially permeable stretching/shrinking sheet. *J. Magn. Magn. Mater.* **2018**, *465*, 365–374. [CrossRef]
12. Mishra, S.; Khan, I.; Al-Mdallal, Q.; Asifa, T. Free convective micropolar fluid flow and heat transfer over a shrinking sheet with heat source. *Case Stud. Therm. Eng.* **2018**, *11*, 113–119. [CrossRef]
13. Khan, K.A.; Butt, A.R.; Raza, N. Effects of heat and mass transfer on unsteady boundary layer flow of a chemical reacting Casson fluid. *Results Phys.* **2018**, *8*, 610–620. [CrossRef]
14. Bibi, M.; Rehman, K.U.; Malik, M.Y.; Tahir, M. Numerical study of unsteady Williamson fluid flow and heat transfer in the presence of MHD through a permeable stretching surface. *Eur. Phys. J. Plus* **2018**, *133*, 154. [CrossRef]
15. Hamid, M.; Usman, M.; Khan, Z.; Ahmad, R.; Wang, W. Dual solutions and stability analysis of flow and heat transfer of Casson fluid over a stretching sheet. *Phys. Lett. A* **2019**, *383*, 2400–2408. [CrossRef]
16. Waini, I.; Ishak, A.; Pop, I. Unsteady flow and heat transfer past a stretching/shrinking sheet in a hybrid nanofluid. *Int. J. Heat Mass Transf.* **2019**, *136*, 288–297. [CrossRef]
17. Sahoo, B.; Shevchuk, I.V. Heat transfer due to revolving flow of Reiner-Rivlin fluid over a stretchable surface. *Therm. Sci. Eng. Prog.* **2019**, *10*, 327–336. [CrossRef]
18. Bibi, M.; Zeeshan, A.; Malik, M.Y.; Rehman, K.U. Numerical investigation of the unsteady solid-particle flow of a tangent hyperbolic fluid with variable thermal conductivity and convective boundary. *Eur. Phys. J. Plus* **2019**, *134*, 298. [CrossRef]
19. Benos, L.; Mahabaleshwar, U.; Sakanaka, P.; Sarris, I. Thermal analysis of the unsteady sheet stretching subject to slip and magnetohydrodynamic effects. *Therm. Sci. Eng. Prog.* **2019**, *13*, 100367. [CrossRef]
20. Ali, U.; Rehman, K.U.; Malik, M.Y. The influence of MHD and heat generation/absorption in a Newtonian flow field manifested with a Cattaneo–Christov heat flux model. *Phys. Scr.* **2019**, *94*, 085217. [CrossRef]
21. Yang, W.; Chen, X.; Zhang, X.; Zheng, L.; Liu, F. Flow and heat transfer of double fractional Maxwell fluids over a stretching sheet with variable thickness. *Appl. Math. Model.* **2020**, *80*, 204–216. [CrossRef]
22. Naganthran, K.; Hashim, I.; Nazar, R. Non-uniqueness solutions for the thin Carreau film flow and heat transfer over an unsteady stretching sheet. *Int. Commun. Heat Mass Transf.* **2020**, *117*, 104776. [CrossRef]
23. Waini, I.; Ishak, A.; Pop, I. Transpiration effects on hybrid nanofluid flow and heat transfer over a stretching/shrinking sheet with uniform shear flow. *Alex. Eng. J.* **2020**, *59*, 91–99. [CrossRef]
24. Khan, A.A.; Ahmed, A.; Askar, S.; Ashraf, M.; Ahmad, H.; Khan, M.N. Influence of the induced magnetic field on second-grade nanofluid flow with multiple slip boundary conditions. *Waves Random Complex Media* **2021**, 1–16. [CrossRef]
25. Bejawada, S.G.; Khan, Z.H.; Hamid, M. Heat generation/absorption on MHD flow of a micropolar fluid over a heated stretching surface in the presence of the boundary parameter. *Heat Transf.* **2021**, *50*, 6129–6147. [CrossRef]
26. Zhang, Y.; Zhang, Y.; Bai, Y.; Yuan, B.; Zheng, L. Flow and heat transfer analysis of a maxwell-power-law fluid film with forced thermal Marangoni convective. *Int. Commun. Heat Mass Transf.* **2021**, *121*, 105062. [CrossRef]
27. Alhamaly, A.; Khan, M.; Shuja, S.; Yilbas, B.; Al-Qahtani, H. Axisymmetric stagnation point flow on linearly stretching surfaces and heat transfer: Nanofluid with variable physical properties. *Case Stud. Therm. Eng.* **2021**, *24*, 100839. [CrossRef]
28. Megahed, A.M. Improvement of heat transfer mechanism through a Maxwell fluid flow over a stretching sheet embedded in a porous medium and convectively heated. *Math. Comput. Simul.* **2021**, *187*, 97–109. [CrossRef]
29. Prasannakumara, B.C. Numerical simulation of heat transport in Maxwell nanofluid flow over stretching sheet considering magnetic dipole effect. *Partial. Differ. Equ. Appl. Math.* **2021**, *4*, 100064. [CrossRef]

30. Megahed, M.A.; Reddy, M.G.; Abbas, W. Modeling of MHD fluid flow over an unsteady stretching sheet with thermal radiation, variable fluid properties and heat flux. *Math. Comput. Simul.* **2021**, *185*, 583–593. [CrossRef]
31. Pearson, J.; Tardy, P. Models for flow of non-Newtonian and complex fluids through porous media. *J. Non-Newton. Fluid Mech.* **2002**, *102*, 447–473. [CrossRef]
32. Eldabe, N.T.; Mohamed, M.A. Heat and mass transfer in hydromagnetic flow of the non-Newtonian fluid with heat source over an accelerating surface through a porous medium. *Chaos Solitons Fractals* **2002**, *13*, 907–917. [CrossRef]
33. Eberhard, U.; Seybold, H.J.; Floriancic, M.; Bertsch, P.; Jiménez-Martínez, J.; Andrade, J.S., Jr.; Holzner, M. Determination of the effective viscosity of non-Newtonian fluids flowing through porous media. *Front. Phys.* **2019**, *7*, 71. [CrossRef]
34. Wang, F.; Rehman, S.; Bouslimi, J.; Khaliq, H.; Qureshi, M.I.; Kamran, M.; Abdulaziz, N.A.; Hijaz, A.; Farooq, A. Comparative study of heat and mass transfer of generalized MHD Oldroyd-B bio-nano fluid in a permeable medium with ramped conditions. *Sci. Rep.* **2021**, *11*, 23454. [CrossRef]
35. Mahabaleshwar, U.; Vishalakshi, A.; Azese, M.N. The role of Brinkmann ratio on non-Newtonian fluid flow due to a porous shrinking/stretching sheet with heat transfer. *Eur. J. Mech.-B/Fluids* **2019**, *92*, 153–165. [CrossRef]
36. Nadeem, S.; Hussain, S.T.; Lee, C. Flow of a Williamson fluid over a stretching sheet. *Braz. J. Chem. Eng.* **2013**, *30*, 619–625. [CrossRef]
37. Abouelregal, A.E.; Ersoy, H.; Civalek, Ö. Solution of Moore–Gibson–Thompson equation of an un-bounded medium with a cylindrical hole. *Mathematics* **2021**, *9*, 1536. [CrossRef]
38. Numanoğlu, H.M.; Ersoy, H.; Akgöz, B.; Civalek, Ö. A new eigenvalue problem solver for thermo-mechanical vibration of Timoshenko nanobeams by an innovative nonlocal finite element method. *Math. Methods Appl. Sci.* **2021**, *in press*. [CrossRef]
39. Rehman, K.U.; Malik, A.A.; Malik, M.; Tahir, M.; Zehra, I. On new scaling group of transformation for Prandtl-Eyring fluid model with both heat and mass transfer. *Results Phys.* **2018**, *8*, 552–558. [CrossRef]
40. Rehman, K.U.; Shatanawi, W.; Shatnawi, T.A.M. On thermal energy transport complications in chemically reactive liquidized flow fields manifested with thermal slip arrangements. *Energies* **2021**, *14*, 8530. [CrossRef]